Letter

Detecting the critical point through entanglement in the Schwinger model

Kazuki Ikeda,[1,2,*] Dmitri E. Kharzeev,[1,2,3,†] René Meyer,[4,5,‡] and Shuzhe Shi[6,2,§]

[1]*Co-design Center for Quantum Advantage, Stony Brook University, Stony Brook, New York 11794-3800, USA*
[2]*Center for Nuclear Theory, Department of Physics and Astronomy, Stony Brook University, Stony Brook, New York 11794-3800, USA*
[3]*Department of Physics, Brookhaven National Laboratory, Upton, New York 11973-5000, USA*
[4]*Institute for Theoretical Physics and Astrophysics, Julius-Maximilians-Universität Würzburg, Am Hubland, 97074 Würzburg, Germany*
[5]*Würzburg-Dresden Cluster of Excellence (ct.qmat)*
[6]*Department of Physics, Tsinghua University, Beijing 100084, China*

(Received 18 May 2023; accepted 13 October 2023; published 9 November 2023)

Using quantum simulations on classical hardware, we study the phase diagram of the massive Schwinger model with a θ term at finite chemical potential μ. We find that the quantum critical point in the phase diagram of the model can be detected through the entanglement entropy and entanglement spectrum. As a first step, we chart the phase diagram using conventional methods by computing the dependence of the charge and chiral condensates on the fermion mass m, coupling constant g, and the chemical potential μ. At zero density, the Schwinger model possesses a quantum critical point at $\theta = \pi$ and $m/g \simeq 0.33$. We find that the position of this quantum critical point depends on the chemical potential. Near this quantum critical point, we observe a sharp maximum in the entanglement entropy. Moreover, we find that the quantum critical point can be located from the entanglement spectrum by detecting the position of the gap closing point.

DOI: 10.1103/PhysRevD.108.L091501

Introduction. The Schwinger model [1] is quantum electrodynamics in $(1+1)$ space-time dimensions. This model shares many properties with QCD, including confinement (in the massive case) and chiral symmetry breaking. For the case of massless fermions, the Schwinger model is analytically solvable and equivalent to the theory of a free massive boson field [1–9]. However, the massive Schwinger model cannot be solved analytically and requires a numerical approach.

Quantum simulations are potentially advantageous for this purpose, as the Hilbert space grows exponentially with the number of lattice sites. In recent years, there has been a growing interest in quantum algorithms as an efficient, and potentially superior, way to explore the dynamics of quantum field theories, including the Schwinger model [10–58]. Another advantage of using quantum algorithms to simulate quantum field theories is the absence of the fermion sign problem at finite chemical potential [59–62].

In the present work, we use classical hardware to simulate the massive Schwinger model at finite temperature and chemical potential. We analyze the entanglement structure of the ground state and demonstrate that entanglement can be used as an efficient diagnostic tool for detecting the phase transition, and in particular the presence of the critical point in the phase diagram.

In particular, we find that, at the critical point, there is a level crossing in the entanglement spectrum. Also, near the critical point, the entanglement entropy for a single spatial interval follows predictions from two-dimensional conformal field theory. It is well known that entanglement is a good probe of topological order [63–65]. Our results suggest that entanglement can be used to detect the fluctuating topology as well.

In [66], we showed that the presence of the critical point in the phase diagram can be detected through a sharp growth of topological fluctuations reflected by the real-time topological susceptibility. In this work, we confirm the presence of the critical point at finite and vanishing chemical potential by a calculation of the topological susceptibility, as well as the charge susceptibility.

*kazuki.ikeda@stonybrook.edu
†dmitri.kharzeev@stonybrook.edu
‡rene.meyer@uni-wuerzburg.de
§shuzhe-shi@tsinghua.edu.cn

$1+1$-*Dimensional qed.* In the presence of finite chemical potential, the Hamiltonian of the massive Schwinger model with a θ term in $(1+1)$-dimensional Minkowski space in temporal gauge $A_0 = 0$ is

$$H = \int dz \left[\frac{E^2}{2} - \bar{\psi}(i\gamma^1\partial_1 - g\gamma^1 A_1 - me^{i\gamma_5\theta} + \mu\gamma^0)\psi \right]. \quad (1)$$

Here, A_μ is the $U(1)$ gauge potential, $E = \dot{A}_1$ is the corresponding electric field, ψ is a two-component fermion field, m is the fermion mass, μ is the chemical potential, and the γ^μ's are two-dimensional γ-matrices satisfying the Clifford algebra. We use the metric convention $\eta_{\mu\nu} = \mathrm{diag}(1,-1)$. From Eq. (1), we see that the massive theory with a positive mass $m > 0$ at $\theta = \pi$ is equivalent to the theory at $\theta = 0$ with a negative mass $-m$.

We first discretize the continuum system to obtain the lattice Hamiltonian as follows: We discretize the spatial coordinate as $z = an$, where a is a lattice constant and n is an integer. We choose to work with staggered fermions [67,68], in which a two-component Dirac fermion $\psi = (\psi^1, \psi^2)^T$ is converted to $\psi^1(\psi^2) \to \chi_n/\sqrt{a}$ for odd (even) n. We further define $L_n = E(an)/g$ and $U_n = e^{-iagA_1(an)}$, respectively, as the gauge field and gauge link operators connecting the nth and $(n+1)$th sites. We define our Dirac matrices as $\gamma^0 = Z$, $\gamma^1 = iY$, and $\gamma^5 = \gamma^0\gamma^1 = X$, where X, Y, and Z are the Pauli matrices. The lattice Hamiltonian then reads

$$H = \sum_{n=1}^{N-1} \left(\frac{im}{2}(-1)^n \sin\theta - \frac{i}{2a} \right) (U_n \chi_{n+1}^\dagger \chi_n - U_n^\dagger \chi_n^\dagger \chi_{n+1}) + \sum_{n=1}^{N} (m(-1)^n \cos\theta - \mu)\chi_n^\dagger \chi_n + \frac{ag^2}{2} \sum_{n=0}^{N} L_n^2. \quad (2)$$

Using an open boundary condition ($\chi_0 = \chi_{N+1} = 0$), we can eliminate the link fields U_n by the gauge transformation $\chi_n \to g_n \chi_n$ and $U_n \to g_{n+1} U_n g_n^\dagger$, with $g_1 = 1$, $g_n = \prod_{m=1}^{n-1} U_m^\dagger$ (see, e.g., [66,69]). Gauge invariance of the theory requires that physical states respect Gauss's law:

$$\partial_z E = g\bar{\psi}\gamma^0\psi. \quad (3)$$

Using (3), we get $L_n - L_{n-1} = Q_n$, where $Q_n = \chi_n^\dagger \chi_n - \frac{1-(-1)^n}{2}$ is the local charge operator. As illustrated in Fig. 1, we set the boundary electric field as $L_0 = -Q/2$, with $Q \equiv \sum_{n=1}^{N} Q_n$ being the total charge. This leads to the solution

$$L_n = -\frac{Q}{2} + \sum_{m=1}^{n} Q_m. \quad (4)$$

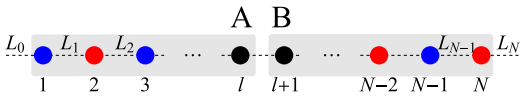

FIG. 1. Illustration of the lattice setup. Red dots are fermions, and blue dots are antifermions. We take the boundary condition as $L_0 = -Q/2$, which leads to $L_N = +Q/2$, with Q being the total charge. See text for explanation.

In this setup, the charge conjugation (C) is equivalent to the parity reflection (P). The P parity is explicitly preserved at $\theta = 0$, and so is C conjugation.

Finally, we use the Jordan-Wigner transformation [70] $\chi_n = \frac{X_n - iY_n}{2} \prod_{m=1}^{n-1}(-iZ_m)$, after which the Hamiltonian becomes

$$H = \sum_{n=1}^{N-1} \left(\frac{1}{4a} - \frac{m}{4}(-1)^n \sin\theta \right) (X_n X_{n+1} + Y_n Y_{n+1}) + \sum_{n=1}^{N} \frac{m(-1)^n \cos\theta - \mu}{2} Z_n + \frac{ag^2}{2} \sum_{n=0}^{N} L_n^2. \quad (5)$$

In our study, we diagonalize this Hamiltonian to obtain eigenstates and compute expectation values.

Phase diagram. The expectation value of an observable O at finite temperature is defined by $\langle O \rangle \equiv \mathrm{Tr}(\rho_{\mathrm{th}} O)$, where the thermal density matrix

$$\rho_{\mathrm{th}} \equiv \frac{e^{-H/T}}{\mathrm{Tr}(e^{-H/T})} \quad (6)$$

is a function of temperature (T), chemical potential, and mass. Observables of interest to us include the total charge ($\langle Q \rangle \equiv \int \langle \psi^\dagger \psi \rangle \mathrm{d}z$), chiral condensate ($\langle \bar{\psi}\psi \rangle \equiv \int \langle \bar{\psi}\psi \rangle dz/L$), and charge susceptibility ($\chi_{Q,2} \equiv (\langle Q \rangle^2 - \langle Q^2 \rangle)/L^2$), with $L = Na$ being the lattice size.

In particular, we study the entanglement entropy between two subsystems $A = \{1, 2, \ldots, \ell\}$ and $B = \{\ell+1, \ldots, N\}$; see Fig. 1, with $A \cap B = \varnothing$, $A \cup B = \{1, 2, \ldots, N\}$. Let ρ be a density operator of the entire system $A \cup B$. The entanglement entropy between A and B is defined by $S_{EE,\ell} \equiv -\mathrm{Tr}_A(\rho_A \log \rho_A)$, where ρ_A is defined by tracing out the Hilbert space of B: $\rho_A = \mathrm{Tr}_B \rho$. The entanglement spectrum, $\{\lambda_i\}$, is spanned by the eigenvalues of ρ_A. In this study, we choose ρ as the ground state of the Hamiltonian, $\rho = |\psi_{gs}\rangle\langle\psi_{gs}|$.

In Fig. 2, we show our results for the thermal expectation values of the charge, chiral condensate, charge fluctuation, and ground-state entanglement entropy ($T = 0$ and $\ell = N/2$) for different values of fermion mass and chemical potential at $T = g/10$ and $\theta = 0$, with lattice parameters $N = 20$, $a = 0.2/g$. Under the charge conjugation $\mu \to -\mu$, we confirm that the total charge is C-odd, $\langle Q \rangle \to -\langle Q \rangle$,

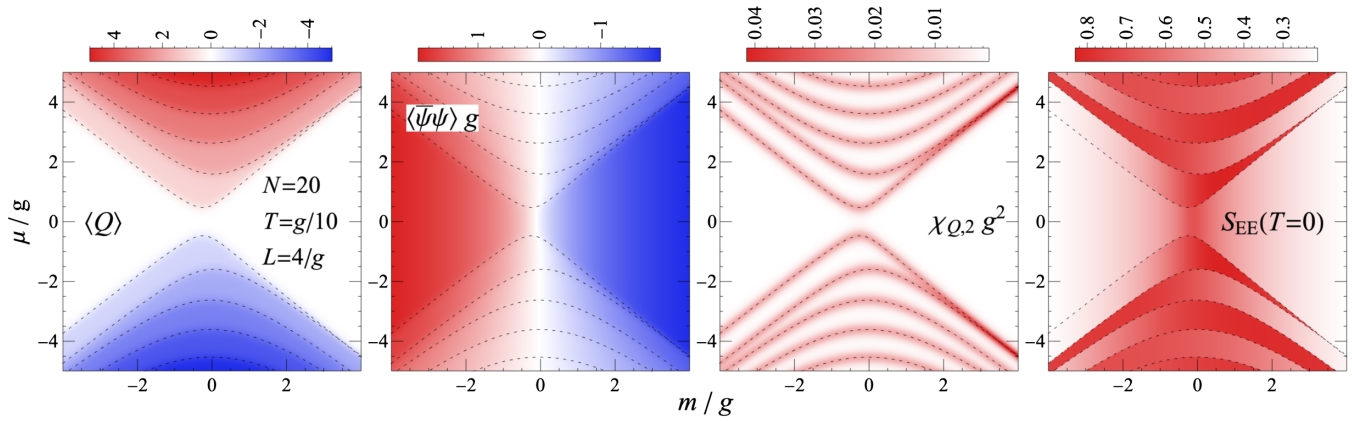

FIG. 2. From left to right: density plot of total charge, chiral condensate, charge fluctuation, and ground-state left-right entanglement entropy for different values of fermion mass and chemical potential, with $N = 20$, $L = 4/g$, and $\theta = 0$. The entanglement entropy is for the ground state, corresponding to $T = 0$, whereas the other panels are for $T = g/10$. The first-order phase transition lines (black dashed contours) are overlaid on top of every panel. See text for more details.

whereas the chiral condensate, second-order charge susceptibility, and entanglement entropy are C-even.

We note that at finite chemical potential, the Hamiltonian (5) can be written as $H(\mu) = H_0 - \mu Q$, where the total charge Q commutes with $H_0 \equiv H(\mu = 0)$, and therefore is a good quantum number. Thus, we may label a quantum state by its energy level and electric charge, $|q, n\rangle$, representing the nth-lowest energy eigenstate that carries q units of charge. We also denote that $H_0|q, n\rangle = E_n^{(q)}|q, n\rangle$ and $Q|q, n\rangle = q|q, n\rangle$. Charge conjugation symmetry requires that $E_n^{(-q)} = E_n^{(q)}$. At vanishing chemical potential, we find that the q-dependent lowest energies follow a hierarchy of charge $E_0^{(q=0)} < E_0^{(|q|=1)} < E_0^{(|q|=2)} < \cdots$, and the gaps between the neighbouring energy levels, $E_0^{(|q|+1)} - E_0^{(|q|)}$, increase with $|q|$. This is caused by the Coulomb repulsive interaction between charged fermions. At finite μ, the energy would be shifted according to the charge, $H(\mu)|q, n\rangle = (E_n^{(q)} - \mu q)|q, n\rangle$. When μ crosses $E_n^{(q=1)} - E_n^{(q=0)}$ from below, the ground state of the system switches from $q = 0$ to $q = 1$. By a similar argument, we find the charge of the ground state to be q in the interval $(E_n^{(q)} - E_n^{(q-1)}) < \mu < (E_n^{(q+1)} - E_n^{(q)})$.

These discrete energy levels depend on the fermion mass m and define the lines of the first-order phase transitions in the phase diagram. These boundaries are shown by black dashed curves in all panels of Fig. 2. These boundaries separate different ground states, and we observe different values of entanglement entropy in each state. At low temperature, $T = g/10$, we observe a clear jump of the total charge across the boundaries, where the charge susceptibility also peaks.

Motivated by the peak in the entanglement entropy in the branch around $\mu = 0$, we investigate the phase with vanishing chemical potential in more detail. We show the entanglement entropy, the scalar condensate, and the charge and topological susceptibilities at $\mu = 0$ in Fig. 3. The topological susceptibility is defined as $\chi_{\mathrm{CS},2} = (\langle q_{\mathrm{CS}}^2\rangle - \langle q_{\mathrm{CS}}\rangle^2)$, where $q_{\mathrm{CS}} = \partial_\mu K^\mu$ is the Chern-Pontryagin number density associated with the divergence of the Chern-Simons current (K^μ). In $(1+1)$ dimensions, $K^\mu = (g/2\pi)\epsilon^{\mu\nu}A_\nu$ and $q_{\mathrm{CS}} = (g/4\pi)\epsilon^{\mu\nu}F_{\mu\nu} = (g/2\pi)E = (g^2/2\pi)\sum_{n=1}^{N-1} L_n/(N-1)$.

We observe that entanglement entropy peaks at $m^* \approx -0.11g$, where the chiral condensate also vanishes.

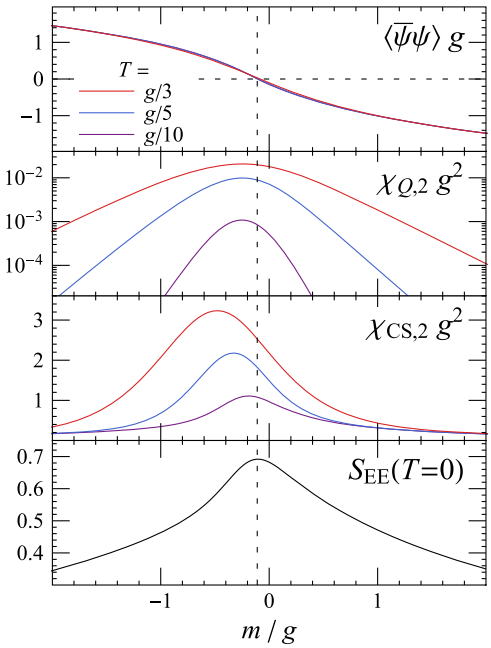

FIG. 3. From top to bottom: fermion mass dependence of chiral condensate, vector charge susceptibility, chiral susceptibility, and vacuum entanglement entropy, with $\theta = 0$ and $\mu = 0$. In the top three panels, red, blue, and purple curves represent $T = g/3$, $g/5$, and $g/10$, respectively.

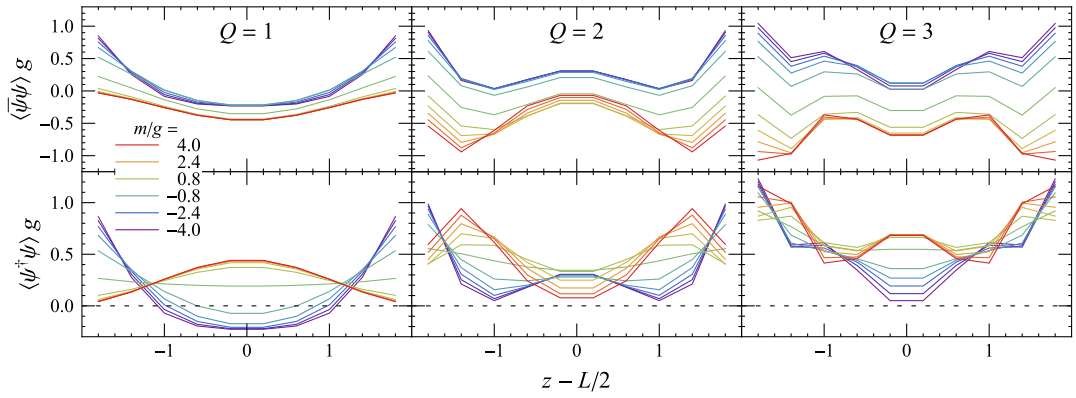

FIG. 4. From left to right: spatial distribution of chiral condensate (upper panel) and charge density (lower panel) for $Q = 1$, 2, and 3 states, with shown values of fermion mass.

Meanwhile, fluctuations of both vector charge and Chern-Simons numbers peak around the same mass m^* at low temperatures. The value of m^* is consistent with previous calculation [66], which takes the real-time topological susceptibility to detect the critical point. We note that the value of the critical point differs from the well-known result at the continuum limit ($\approx -0.33g$) [71–73] due to the effects of finite lattice spacing [74] and finite volume (See Appendix A).

The coincidence of the critical point of the phase diagram with the peak of the entanglement entropy is known for some models. For example, it is suggested that entanglement measures are suitable tools for analyzing phase transitions in spin systems [75,76]. However, as stressed in [75], the discontinuity in entanglement entropy is not always related to a first-order phase transition.

In the $\mu \neq 0$ branches of the phase diagram in Fig. 2, we observe that entanglement entropy monotonically increases (decreases) with mass for odd (even) charge. This is due to the mass dependence of the charge density in the middle of the system, at the boundary of subsystems A and B; see lower panels in Fig. 4. For finite chemical potential, we see a hint of the crystalline structure discussed in [77–79] in Fig. 4.

In a conformal field theory on a finite interval of length $L = aN$, the entanglement entropy of a subsystem with length $\ell = al$ and its complement obeys [80]

$$S_{EE,l} = \frac{c}{6}\ln\left(\frac{2N}{\pi}\sin\frac{\pi l}{N}\right) - c', \tag{7}$$

where c is the central charge. It is known that the massive Schwinger model at critical mass m^* is a conformal fixed point and belongs to the universality class of the classical 2D Ising model, in which the central charge is expected to approach $c = 1$ in the continuum limit. In what follows, we study the entanglement entropy between the subsystems A and B are defined as in Fig. 1, where the length of A is taken to be ℓ. We study the finite-size effects in the entanglement entropy by varying the lattice spacing (a) and number of lattice sites (N). For each choice of a and N, we first determine the critical mass by maximizing S_{EE} when $l = N/2$ and then compute $S_{EE,l}$ at different values of l. We refer to Fig. 8 for more details. By fitting the results using Eq. (7), we obtain the central charge (see Fig. 5). It is clear that the l dependence of $S_{EE,l}$ is well described by (7), and the corresponding central charge is within ∼15% from $c = 1$. We suspect that the deviation from $c = 1$ is caused by finite-size effects, as the continuum limit $ag \to 0$ in Fig. 5 is beyond the reach of our numerical capacity. This is supported by the fact that c seems to approach unity when the lattice spacing decreases and the number of sites increases.

Finally, we study the entanglement spectrum. Suppose that the dimension of the Hilbert space of subsystem A is not larger than that of subsystem B: $\dim \mathcal{H}_A \leq \dim \mathcal{H}_B$. The Gram-Schmidt orthonormalization of a quantum state is

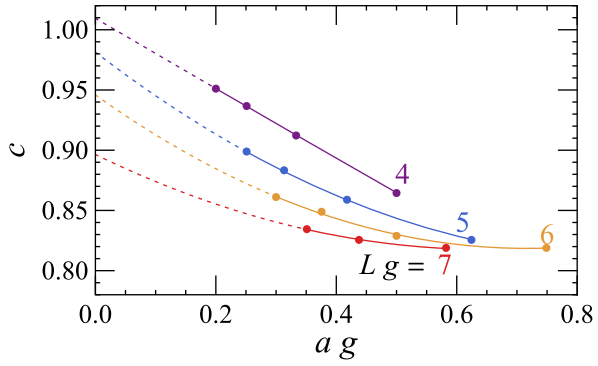

FIG. 5. Central charge versus lattice spacing. Purple, blue, orange, and red symbols correspond to lengths $L = 4/g$, $5/g$, $6/g$, and $7/g$, respectively. The dashed curves are second-order polynomial fits to guide the eye. They come close to the expected central charge $c = 1$ in the continuum limit $a \to 0$ within 15% accuracy. Results are evaluated at vanishing chemical potential.

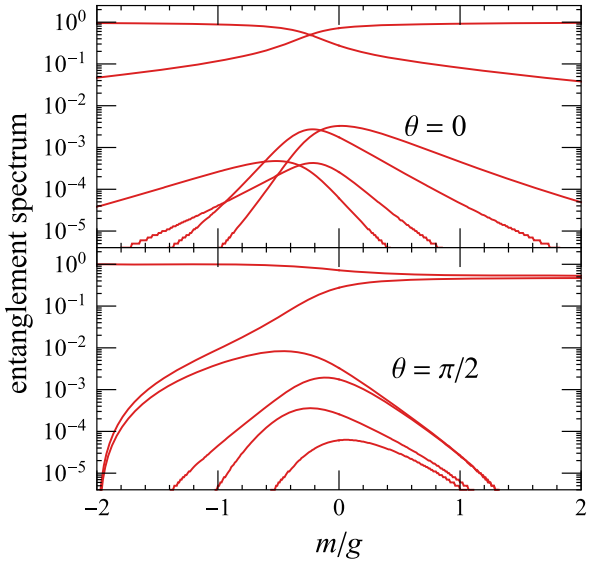

FIG. 6. Entanglement spectrum at $\theta = 0$ (upper panel) and $\theta = \pi/2$ (lower panel). Other parameters are set to $N = 10$, $a = 0.5/g$, and $\mu = 0$.

$$|\psi\rangle = \sum_{\alpha=1}^{\dim \mathcal{H}_A} \xi_\alpha |\psi_\alpha^A\rangle_A |\psi_\alpha^B\rangle_B, \tag{8}$$

and the coefficients ξ_α ($\alpha = 1, \ldots, \dim \mathcal{H}_A$) constitute the entanglement spectrum [64].

Our simulations show that the gap in the entanglement spectrum closes at the critical point—i.e., at $m^* \simeq -0.11g$; see the upper panel of Fig. 6. We present the results at $\mu = 0$, but we find similar band-crossing points in the entanglement spectrum at finite chemical potential as well. The parity symmetry in the Schwinger model is broken if $\theta \neq 0, \pi$ due to the background electric field, which results in a nonzero gap in the entanglement spectrum. We confirm this by showing in the lower panel of Fig. 6 the entanglement spectrum at $\theta = \pi/2$.

To summarize, we have performed a quantum simulation of the massive Schwinger model at finite chemical potential and temperature, and have found that the location of the critical point in the phase diagram can be determined from the entanglement entropy and the entanglement spectrum. The entanglement entropy peaks in the vicinity of the critical point, showing conformal behavior. The entanglement spectrum near the critical point exhibits the level-crossing phenomenon in the first- and second-highest spectra. The latter correspond to the lowest eigenvalues of the entanglement Hamiltonian, which are most relevant in the thermodynamic limit of large system size. We speculate that the entanglement entropy and entanglement spectrum show a similar behavior near the critical points in other, more complicated field theories, including QCD. It would be interesting to confirm these findings in other theories, such as holographic QCD [81,82], and to investigate whether the symmetry-resolved entanglement [83] in the Schwinger model can indicate the presence of the critical point as well.

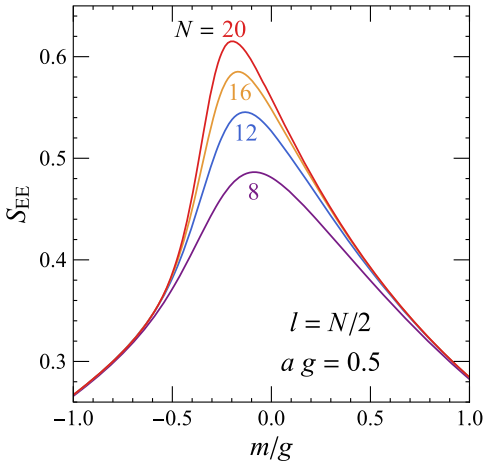

FIG. 7. Entanglement entropy versus the fermion mass with the number of lattice sites being $N = 8$ (purple), 12 (blue), 16 (orange), and 20 (red). Lattice spacing is fixed to be $a = 0.5/g$.

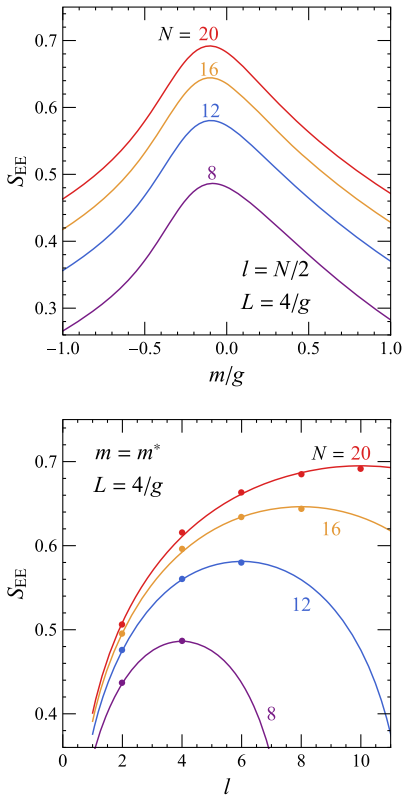

FIG. 8. Mass (top) and length (bottom) dependence of entanglement entropy. Curves in the middle panel are fitted results using Eq. (7). Purple, blue, orange, and red curves correspond to total numbers of lattice sites $N = 8$, 12, 16, and 20, respectively. Results are evaluated at vanishing chemical potential.

Acknowledgments. We thank Giuseppe Di Giulio and Vladimir Korepin for useful discussions. This work was supported by the U.S. Department of Energy, Office of Science, National Quantum Information Science Research Centers, Co-design Center for Quantum Advantage (C2QA) under Contract No. DE-SC0012704 (K. I., D. K.), and the U.S. Department of Energy, Office of Science, Office of Nuclear Physics, Grants No. DE-FG88ER41450 (D. K., S. S.), No. DE-SC0012704 (D. K.), and Tsinghua University under Grant No. 53330500923 (S. S.). The work of R. M. was supported by the Deutsche Forschungsgemeinschaft (DFG, German Research Foundation) through Project-ID No. 258499086-SFB 1170 "ToCoTronics" and through the Würzburg-Dresden Cluster of Excellence on Complexity and Topology in Quantum Matter—ct.qmat Project-ID 390858490—EXC 2147.

Appendix A: Finite-volume effect. In the main text, we take the numerical setting with number of sites $N = 20$ and total volume $L = 4/g$ and find the critical point to be $m^* = -0.11g$. Its deviation from the well-known result for the Schwinger model in continuum ($-0.33g$) is caused by the effects of finite lattice spacing and volume. In Fig. 7, we show the entanglement entropy with various lattice volume (fixed spacing but various numbers of sites). It is clear that as volume increases, the peak becomes sharper, and the position of the peak approaches its continuum limit.

Appendix B: Central charge determination. Here we supplement more details for Fig. 5 of the main text, where we present the result of central charge (c) at various lattice spacings (a) and numbers of sites (N). We take a system with length $L = 4/g$ as an example. For each choice of a and N, we first determine the critical mass (m^*) by maximizing S_{EE} when $l = N/2$; see Fig. 8 (top). Then, we take $m = m^*$ and compute $S_{EE,l}$ at different values of l, which are presented as dots in Fig. 8 (bottom). Finally, the l dependence of S_{EE} is fitted according to Eq. (7) of the main text, and the best-fit results are also shown in Fig. 8 (bottom).

[1] J. S. Schwinger, Gauge invariance and mass, Phys. Rev. **125**, 397 (1962).
[2] L. Brown, Gauge invariance and mass in a two-dimensional model, Nuovo Cimento (1955–1965) **29**, 617 (1963).
[3] C. M. Sommerfield, On the definition of currents and the action principle in field theories of one spatial dimension, Ann. Phys. (N.Y.) **26**, 1 (1964).
[4] B. Zumino, Charge conservation and the mass of the photon, Phys. Lett. **10**, 224 (1964).
[5] C. Hagen, Current definition and mass renormalization in a model field theory, Il Nuovo Cimento A (1965–1970) **51**, 1033 (1967).
[6] J. Lowenstein and J. Swieca, Quantum electrodynamics in two dimensions, Ann. Phys. (N.Y.) **68**, 172 (1971).
[7] A. Casher, J. Kogut, and L. Susskind, Vacuum polarization and the absence of free quarks, Phys. Rev. D **10**, 732 (1974).
[8] S. Coleman, R. Jackiw, and L. Susskind, Charge shielding and quark confinement in the massive Schwinger model, Ann. Phys. (N.Y.) **93–2**, 267 (1975).
[9] A. Tomiya, Schwinger model at finite temperature and density with beta VQE, arXiv:2205.08860.
[10] A. Wallraff, D. I. Schuster, A. Blais, L. Frunzio, R. S. Huang, J. Majer, S. Kumar, S. M. Girvin, and R. J. Schoelkopf, Strong coupling of a single photon to a superconducting qubit using circuit quantum electrodynamics, Nature (London) **431**, 162 (2004).
[11] J. Majer, J. M. Chow, J. M. Gambetta, J. Koch, B. R. Johnson, J. A. Schreier, L. Frunzio, D. I. Schuster, A. A. Houck, A. Wallraff, A. Blais, M. H. Devoret, S. M. Girvin, and R. J. Schoelkopf, Coupling superconducting qubits via a cavity bus, Nature (London) **449**, 443 (2007).
[12] S. P. Jordan, K. S. M. Lee, and J. Preskill, Quantum algorithms for quantum field theories, Science **336**, 1130 (2012).
[13] S. P. Jordan, K. S. M. Lee, and J. Preskill, Quantum computation of scattering in scalar quantum field theories, Quantum Inf. Comput. **14**, 1014 (2014).
[14] E. Zohar, J. I. Cirac, and B. Reznik, Simulating compact quantum electrodynamics with ultracold atoms: Probing confinement and nonperturbative effects, Phys. Rev. Lett. **109**, 125302 (2012).
[15] E. Zohar, J. I. Cirac, and B. Reznik, Cold-atom quantum simulator for SU(2) Yang-Mills lattice gauge theory, Phys. Rev. Lett. **110**, 125304 (2013).
[16] D. Banerjee, M. Bögli, M. Dalmonte, E. Rico, P. Stebler, U. J. Wiese, and P. Zoller, Atomic quantum simulation of U(N) and SU(N) non-Abelian lattice gauge theories, Phys. Rev. Lett. **110**, 125303 (2013).
[17] D. Banerjee, M. Dalmonte, M. Muller, E. Rico, P. Stebler, U. J. Wiese, and P. Zoller, Atomic quantum simulation of dynamical gauge fields coupled to fermionic matter: From string breaking to evolution after a quench, Phys. Rev. Lett. **109**, 175302 (2012).
[18] U.-J. Wiese, Ultracold quantum gases and lattice systems: Quantum simulation of lattice gauge theories, Ann. Phys. (Amsterdam) **525**, 777 (2013).
[19] U.-J. Wiese, Towards quantum simulating QCD, Nucl. Phys. A **931**, 246 (2014).
[20] S. P. Jordan, K. S. M. Lee, and J. Preskill, Quantum algorithms for fermionic quantum field theories, arXiv:1404.7115.
[21] L. García-Álvarez, J. Casanova, A. Mezzacapo, I. L. Egusquiza, L. Lamata, G. Romero, and E. Solano,

Fermion-fermion scattering in quantum field theory with superconducting circuits, Phys. Rev. Lett. **114**, 070502 (2015).
[22] D. Marcos, P. Widmer, E. Rico, M. Hafezi, P. Rabl, U. J. Wiese, and P. Zoller, Two-dimensional lattice gauge theories with superconducting quantum circuits, Ann. Phys. (Amsterdam) **351**, 634 (2014).
[23] A. Bazavov, Y. Meurice, S.-W. Tsai, J. Unmuth-Yockey, and J. Zhang, Gauge-invariant implementation of the Abelian Higgs model on optical lattices, Phys. Rev. D **92**, 076003 (2015).
[24] E. Zohar, J. I. Cirac, and B. Reznik, Quantum simulations of lattice gauge theories using ultracold atoms in optical lattices, Rep. Prog. Phys. **79**, 014401 (2016).
[25] A. Mezzacapo, E. Rico, C. Sabín, I. L. Egusquiza, L. Lamata, and E. Solano, Non-Abelian $SU(2)$ lattice gauge theories in superconducting circuits, Phys. Rev. Lett. **115**, 240502 (2015).
[26] M. Dalmonte and S. Montangero, Lattice gauge theory simulations in the quantum information era, Contemp. Phys. **57**, 388 (2016).
[27] E. Zohar, A. Farace, B. Reznik, and J. I. Cirac, Digital lattice gauge theories, Phys. Rev. A **95**, 023604 (2017).
[28] E. A. Martinez *et al.*, Real-time dynamics of lattice gauge theories with a few-qubit quantum computer, Nature (London) **534**, 516 (2016).
[29] A. Bermudez, G. Aarts, and M. Müller, Quantum sensors for the generating functional of interacting quantum field theories, Phys. Rev. X **7**, 041012 (2017).
[30] J. M. Gambetta, J. M. Chow, and M. Steffen, Building logical qubits in a superconducting quantum computing system, npj Quantum Inf. **3**, 2 (2017).
[31] L. Krinner, M. Stewart, A. Pazmiño, J. Kwon, and D. Schneble, Spontaneous emission of matter waves from a tunable open quantum system, Nature (London) **559**, 589 (2018).
[32] A. Macridin, P. Spentzouris, J. Amundson, and R. Harnik, Electron-phonon systems on a universal quantum computer, Phys. Rev. Lett. **121**, 110504 (2018).
[33] T. V. Zache, F. Hebenstreit, F. Jendrzejewski, M. K. Oberthaler, J. Berges, and P. Hauke, Quantum simulation of lattice gauge theories using Wilson fermions, Sci. Technol. **3**, 034010 (2018).
[34] J. Zhang, J. Unmuth-Yockey, J. Zeiher, A. Bazavov, S. W. Tsai, and Y. Meurice, Quantum simulation of the universal features of the Polyakov loop, Phys. Rev. Lett. **121**, 223201 (2018).
[35] N. Klco, E. F. Dumitrescu, A. J. McCaskey, T. D. Morris, R. C. Pooser, M. Sanz, E. Solano, P. Lougovski, and M. J. Savage, Quantum-classical computation of Schwinger model dynamics using quantum computers, Phys. Rev. A **98**, 032331 (2018).
[36] N. Klco and M. J. Savage, Digitization of scalar fields for quantum computing, Phys. Rev. A **99**, 052335 (2019).
[37] H.-H. Lu *et al.*, Simulations of subatomic many-body physics on a quantum frequency processor, Phys. Rev. A **100**, 012320 (2019).
[38] N. Klco and M. J. Savage, Minimally-entangled state preparation of localized wavefunctions on quantum computers, Phys. Rev. A **102**, 012612 (2020).
[39] H. Lamm and S. Lawrence, Simulation of nonequilibrium dynamics on a quantum computer, Phys. Rev. Lett. **121**, 170501 (2018).
[40] E. Gustafson, Y. Meurice, and J. Unmuth-Yockey, Quantum simulation of scattering in the quantum Ising model, Phys. Rev. D **99**, 094503 (2019).
[41] N. Klco, J. R. Stryker, and M. J. Savage, SU(2) non-Abelian gauge field theory in one dimension on digital quantum computers, Phys. Rev. D **101**, 074512 (2020).
[42] A. Alexandru, P. F. Bedaque, H. Lamm, and S. Lawrence (NuQS Collaboration), σ models on quantum computers, Phys. Rev. Lett. **123**, 090501 (2019).
[43] A. Alexandru, P. F. Bedaque, S. Harmalkar, H. Lamm, S. Lawrence, and N. C. Warrington (NuQS Collaboration), Gluon field digitization for quantum computers, Phys. Rev. D **100**, 114501 (2019).
[44] N. Mueller, A. Tarasov, and R. Venugopalan, Deeply inelastic scattering structure functions on a hybrid quantum computer, Phys. Rev. D **102**, 016007 (2020).
[45] H. Lamm, S. Lawrence, and Y. Yamauchi (NuQS Collaboration), Parton physics on a quantum computer, Phys. Rev. Res. **2**, 013272 (2020).
[46] G. Magnifico, M. Dalmonte, P. Facchi, S. Pascazio, F. V. Pepe, and E. Ercolessi, Real time dynamics and confinement in the Z_n Schwinger-Weyl lattice model for $1+1$ QED, Quantum **4**, 281 (2020).
[47] B. Chakraborty, M. Honda, T. Izubuchi, Y. Kikuchi, and A. Tomiya, Digital quantum simulation of the Schwinger model with topological term via adiabatic state preparation, Phys. Rev. D **105**, 094503 (2022).
[48] D. E. Kharzeev and Y. Kikuchi, Real-time chiral dynamics from a digital quantum simulation, Phys. Rev. Res. **2**, 023342 (2020).
[49] A. F. Shaw, P. Lougovski, J. R. Stryker, and N. Wiebe, Quantum algorithms for simulating the lattice Schwinger model, Quantum **4**, 306 (2020).
[50] B. Şahinoğlu and R. D. Somma, Hamiltonian simulation in the low energy subspace, npj Quantum Inf. **7**, 119 (2021).
[51] D. Paulson *et al.*, Towards simulating 2D effects in lattice gauge theories on a quantum computer, PRX Quantum **2**, 030334 (2021).
[52] S. V. Mathis, G. Mazzola, and I. Tavernelli, Toward scalable simulations of lattice gauge theories on quantum computers, Phys. Rev. D **102**, 094501 (2020).
[53] Y. Ji, H. Lamm, and S. Zhu (NuQS Collaboration), Gluon field digitization via group space decimation for quantum computers, Phys. Rev. D **102**, 114513 (2020).
[54] I. Raychowdhury and J. R. Stryker, Loop, string, and hadron dynamics in SU(2) Hamiltonian lattice gauge theories, Phys. Rev. D **101**, 114502 (2020).
[55] Z. Davoudi, I. Raychowdhury, and A. Shaw, Search for efficient formulations for Hamiltonian simulation of non-Abelian lattice gauge theories, Phys. Rev. D **104**, 074505 (2021).
[56] R. Dasgupta and I. Raychowdhury, Cold atom quantum simulator for string and hadron dynamics in non-Abelian lattice gauge theory, Phys. Rev. A **105**, 023322 (2022).
[57] G. Magnifico, D. Vodola, E. Ercolessi, S. P. Kumar, M. Müller, and A. Bermudez, Symmetry-protected topological

phases in lattice gauge theories: Topological QED_2, Phys. Rev. D **99**, 014503 (2019).
[58] K. Ikeda, Criticality of quantum energy teleportation at phase transition points in quantum field theory, Phys. Rev. D **107**, L071502 (2023).
[59] R. P. Feynman, Simulating physics with computers, Int. J. Theor. Phys. **21**, 467 (1982).
[60] J. Preskill, Simulating quantum field theory with a quantum computer, Proc. Sci., LATTICE2018 (**2018**) 024 [arXiv:1811.10085].
[61] S. P. Jordan, K. S. M. Lee, and J. Preskill, Quantum algorithms for quantum field theories, Science **336**, 1130 (2012).
[62] J. Preskill, Quantum computing 40 years later, arXiv:2106.10522.
[63] H.-C. Jiang, Z. Wang, and L. Balents, Identifying topological order by entanglement entropy, Nat. Phys. **8**, 902 (2012).
[64] F. Pollmann, A. M. Turner, E. Berg, and M. Oshikawa, Entanglement spectrum of a topological phase in one dimension, Phys. Rev. B **81**, 064439 (2010).
[65] N. Mueller, T. V. Zache, and R. Ott, Thermalization of gauge theories from their entanglement spectrum, Phys. Rev. Lett. **129**, 011601 (2022).
[66] K. Ikeda, D. E. Kharzeev, and Y. Kikuchi, Real-time dynamics of Chern-Simons fluctuations near a critical point, Phys. Rev. D **103**, L071502 (2021).
[67] J. B. Kogut and L. Susskind, Hamiltonian formulation of Wilson's lattice gauge theories, Phys. Rev. D **11**, 395 (1975).
[68] L. Susskind, Lattice fermions, Phys. Rev. D **16**, 3031 (1977).
[69] A. Florio, D. Frenklakh, K. Ikeda, D. Kharzeev, V. Korepin, S. Shi, and K. Yu, Real-time non-perturbative dynamics of jet production: Quantum entanglement and vacuum modification, Phys. Rev. Lett. **131**, 021902 (2023).
[70] P. Jordan and E. P. Wigner, About the Pauli exclusion principle, Z. Phys. **47**, 631 (1928).
[71] A. Schiller and J. Ranft, The massive Schwinger model on the lattice studied via a local Hamiltonian Monte Carlo method, Nucl. Phys. B **225**, 204 (1983).
[72] C. J. Hamer, J. B. Kogut, D. P. Crewther, and M. M. Mazzolini, The massive Schwinger model on a lattice: Background field, chiral symmetry and the string tension, Nucl. Phys. B **208**, 413 (1982).
[73] T. Byrnes, P. Sriganesh, R. J. Bursill, and C. J. Hamer, Density matrix renormalization group approach to the massive Schwinger model, Phys. Rev. D **66**, 013002 (2002).
[74] R. Dempsey, I. R. Klebanov, S. S. Pufu, and B. Zan, Discrete chiral symmetry and mass shift in the lattice Hamiltonian approach to the Schwinger model, Phys. Rev. Res. **4**, 043133 (2022).
[75] M. Filippone, S. Dusuel, and J. Vidal, Quantum phase transitions in fully connected spin models: An entanglement perspective, Phys. Rev. A **83**, 022327 (2011).
[76] Y. Susa, J. F. Jadebeck, and H. Nishimori, Relation between quantum fluctuations and the performance enhancement of quantum annealing in a nonstoquastic Hamiltonian, Phys. Rev. A **95**, 042321 (2017).
[77] W. Fischler, J. B. Kogut, and L. Susskind, Quark confinement in unusual environments, Phys. Rev. D **19**, 1188 (1979).
[78] Y.-C. Kao and Y.-W. Lee, Inhomogeneous chiral condensate in the Schwinger model at finite density, Phys. Rev. D **50**, 1165 (1994).
[79] S. Nagy, J. Polonyi, and K. Sailer, Periodic ground state for the charged massive Schwinger model, Phys. Rev. D **70**, 105023 (2004).
[80] P. Calabrese and J. Cardy, Entanglement entropy and conformal field theory, J. Phys. A **42**, 504005 (2009).
[81] T. Sakai and S. Sugimoto, Low energy hadron physics in holographic QCD, Prog. Theor. Phys. **113**, 843 (2005).
[82] H.-U. Yee and I. Zahed, Holographic two dimensional QCD and Chern-Simons term, J. High Energy Phys. 07 (2011) 033.
[83] M. Goldstein and E. Sela, Symmetry-resolved entanglement in many-body systems, Phys. Rev. Lett. **120**, 200602 (2018).